Helium ion microscopy of lepidoptera scales

Stuart A. Boden*, Asa Asadollahbaik, Harvey N. Rutt, Darren M. Bagnall

Electronics and Computer Science, University of Southampton, Highfield, Southampton, Hampshire, UK, SO17 1BJ

*corresponding author, sb1@ecs.soton.ac.uk

Key words: Helium ion microscopy, scanning electron microscopy, structural color, charge neutralization, stereo pairs

1 Abstract

In this report, helium ion microscopy (HIM) is used to study the micro and nano-structures responsible for structural color in the wings of two species of Lepidotera from the Papilionidae family: *Papilio ulysses* (Blue Mountain Butterfly) and *Parides sesostris* (Emerald-patched Cattleheart). Electronic charging under the beam of uncoated scales from the wings of these butterflies is successfully neutralized, leading to images displaying a large depth-of-field and a high level of surface detail, which would normally be obscured by traditional coating methods used for scanning electron microscopy (SEM). The images are compared to those from variable pressure SEM, demonstrating the superiority of HIM at high magnifications. In addition, the large depth-of-field capabilities of HIM are exploited through the creation of stereo pairs which allows the exploration of the third dimension. Furthermore, the extraction of quantitative height information which matches well with cross-sectional transmission electron microscopy (TEM) measurements from the literature is demonstrated.

2 Introduction

The huge diversity of colors observed in nature has been a source of fascination throughout human history. The visual appearance of most biological systems is governed by the distribution of pigments, chemicals that selectively absorb part of the spectrum of white light. Perhaps the most striking colors however are produced by entirely different mechanisms based on spatial variations in refractive index on the order of the wavelength of incident light. Termed “structural color”, this has garnered particular attention because it provides nature with ways to create a variety of remarkable optical effects that would be impossible through the use of pigments alone. Several reviews are available on this topic, detailing examples of structural color observed across the animal and plant kingdoms (Vukusic 2003; Parker 2000; Kinoshita 2005). These range from the vibrant metallic sheen of some Coleoptera (beetles) (Kurachi 2002; Parker 1998; Seago 2009), through the dramatically-colored wing interference patterns found on the transparent wings of some Hymenoptera and Diptera (wasps and flies) (Shevtsova 2011) and to the vivid and often iridescent examples of avian skin (Prum 2003; Prum 1999). Various nanostructures are employed to create these stunning optical effects including thin film multilayers, diffraction gratings, two-dimensional and three-dimensional photonic crystals, either alone or in combination. These are examples of the evolution of structural color driven by natural selection pressures where conspicuousness and vividness are advantageous in attracting potential mates. There are other examples where the survival advantage conferred by camouflage has driven the evolution of antireflective structures, such as the nipple arrays found on the eyes and wings of some species of moth (Bernhard 1967; Yoshida 1996) and the wings of some cicada (Stoddart 2006). Indeed, these represent two of a whole host of structural color examples found in Lepidoptera (the large order of insects that includes moths and butterflies), which have been studied in great detail (Bálint 2004; Vukusic 2000; Yoshioka 2008; Ghiradella 1994). By investigating the nature of the structural color mechanisms at play in Lepidoptera, researchers hope to gain further insights into their development and behaviour. Additionally, after millions of years of optimization through evolution, the natural world may offer effective designs for new biomimetic optical devices that exploit structural color mechanisms to control light (Parker 2007; Watanabe 2005; Boden 2008). Possible applications include

antireflective structures for solar cells (Boden 2010), anti-counterfeiting on banknotes (Berthier 2006) and for artistic decoration on, for example, furniture (Vigneron 2006).

Although light microscopy can be used to characterize the effects of structural coloration in the form of direct imaging and microspectrophotometry (Vukusic 2009; Yoshioka 2006), it is not generally useful for investigating the form of the structures themselves because of their subwavelength scale. Hence electron microscopy, with its superior resolution, has been extensively employed for characterization of these structures. TEM has proved useful in obtaining high resolution cross-sectional images of biological structures, and has the advantage of revealing internal structures that may not be apparent in surface imaging. However, as it relies on a projection image formation method, only two-dimensional information can be obtained from a single image. With TEM 3D tomography, using multiple images combined with computer modelling, it is possible to successfully characterize three dimensional structures in butterfly wings (Argyros 2002; Michielsen 2008). However, TEM sample preparation is difficult and time-consuming as the sample has to be fixed, stained and embedded in resin before a thin (<100 nm) section is prepared. Sample preparation for SEM is far less arduous than for TEM and the technique provides an easily-interpretable, three-dimensional view of the biological structures. Therefore, despite poorer resolution compared to TEM, SEM is used extensively for structural color characterization. Sections from Lepidoptera wings are generally dry (and so vacuum compatible) and simple slicing techniques using razor blades are often sufficient to expose sub-surface structure for SEM imaging (Vukusic 2009). More controllable cyrosectioning can also be employed for this, as can focused-ion-beam cross-sectioning for site-specific exposure of underlying structures (Stavenga 2004; Vukusic 2009).

One aspect of electron microscopy that must be addressed when attempting to image biological samples is specimen charging. The carbon-based chitin polymer, of which most structural color structures are formed, is an insulator and therefore charge accumulates in the vicinity of the beam impact site. This raises the local potential with respect to the material around the impact site, affecting the emission of secondary electrons and even the beam electron trajectories, resulting in deterioration in quality of the SEM image through the appearance of charging artefacts.

Several techniques are used to combat charging effects when imaging insulating materials in an SEM. The most widely used method is to coat the sample with a layer of conducting material, a few nanometres in thickness, by evaporation or sputtering. The coating, usually a high atomic number metal such as Cr, W, Pt, Ir or metal alloy such as Au/Pd, acts as a grounding plane to eliminate the fields associated with charging. With careful control of the thickness, the resolution can even be increased due to extra mass-thickness contrast at the edges of coated structures. There are however several drawbacks with this approach: Achieving a thin and uniform coating over the sample can be difficult, especially when the sample exhibits a high degree of surface topography, as is common with biological structural color features, which can lead to self-shadowing artefacts. These can however be minimized by tilting and rotating the sample during coating (Goldstein 2003). The addition of a coating inherently alters the sample from its true uncoated form and it can be difficult at high magnifications to discriminate between the true characteristics of the sample and artefacts from the coating (Bazou 2010). The granular structure of the coating material is often visible in high resolution SEM images of coated biological specimens and much effort has been spent on the development of coatings with small grain sizes to minimize this effect (Schatten 2011; Chen 1995).

Charging effects associated with SEM of insulating specimens can be mitigated without coating by using low accelerating voltages. Reducing the beam energy from the standard operating value of 10-20 keV causes the emission of secondary and backscattered electrons to initially increase and the beam current to decrease until a point is reached for which the charge entering and exiting the sample is balanced (Goldstein 2003). The exact neutrality point differs between materials but modern SEMs allow effective operation at low beam energies and fine adjustments of beam energy in this range, enabling the search for the neutrality point and therefore the elimination of unwanted charging phenomena. However, careful control of the balance of charges in this way is difficult to achieve and varies with tilt angle as well as beam energy. Furthermore, the energy spread of the electron gun

increases at low beam energies, resulting in degradation of the electron-optical performance due to higher chromatic aberration. This can however be mitigated using beam deceleration techniques whereby the source emits at a high voltage but a negative bias is applied to the sample to reduce the landing voltage (Phifer 2009). Low voltage SEM imaging is also more susceptible to hydrocarbon contamination (Postek 2006). Biological samples are not easily cleaned due to their sensitivity to plasma cleaning techniques and so the build-up of hydrocarbons during imaging can be a significant problem, especially at high magnifications.

The development of SEMs that can operate with chamber pressures considerably greater than those associated with typical high vacuum conditions has led to a third way of overcoming charging problems for insulating samples. Environmental or variable pressure SEMs (E/VP SEMs) contain differential apertures to isolate the column vacuum from that of the chamber, allowing the latter to be up to 1000 times that of the former (Robinson 1974). By introducing a gas such as helium or nitrogen into the chamber, collisions of secondary electrons with the gas molecules result in ionization events that produce positive ions and more electrons. An insulating sample will normally acquire a negative charge during imaging and SE detectors can be positively biased so that positive ions will be accelerated towards the sample, neutralizing the negatively charged regions. The main advantage of this technique is that it is self-regulating and therefore charge neutralization is easily achieved without the need for continuous adjustment. However, the technique suffers from a decreased signal-to-noise ratio because of the scattering of the incident beam by the gas molecules. Higher beam energies are generally used to increase the mean free path of beam electrons through the gas and so reduce scattering but this is at the expense of reduced surface detail that low kV SEM can provide.

In recent years, scanning helium ion microscopy (HIM) has emerged as a new imaging technique with all the advantages of SEM's simple sample preparation procedures and easily interpretable, three dimensional results but with the added benefit of superior resolution and depth-of-field (Ward 2006; Scipioni 2008). Charging also affects HIM, with insulating samples quickly acquiring a positive charge during imaging due to the positively charged incident beam and the flow of negative charges out of the sample in the form of SEs. The positive charge that develops suppresses the outgoing SEs resulting in a dramatic reduction in contrast in images of the insulating region of the sample. This problem however can be easily remedied using an electron flood gun mounted in the HIM chamber. Electron flood guns have been used to reduce surface charging in x-ray photoelectron spectroscopy (Huchital 1972), focused ion beam (Utlaut 2007) and secondary ion mass spectrometry (Gilmore 2003) techniques for many years. In HIM, an integrated electron flood gun can be used to deliver a diffuse beam of low energy electrons to the area being imaged between successive scans (or lines of a scan). The low energy electrons are attracted to the area of the sample that is acquiring a positive charge under the primary beam. Careful adjustment of the flood gun parameters including electron energy, flood time and deflection can lead to effective charge neutralization enabling high-contrast imaging of uncoated, insulating samples. This charge neutralization technique has previously been demonstrated by Bazou *et al.* for HIM imaging of human colon cancer cells (Bazou 2010).

For this work, HIM has been employed to image a range of uncoated biological structures responsible for producing structural color in Lepidoptera wing scales. An electron flood gun is used for charge neutralization to provide high-contrast images of uncoated, insulating samples, with a high level of surface detail. In addition, the large depth-of-field offered by the HIM is exploited to access the third dimension through the creation of stereo pairs (Wells 1960).

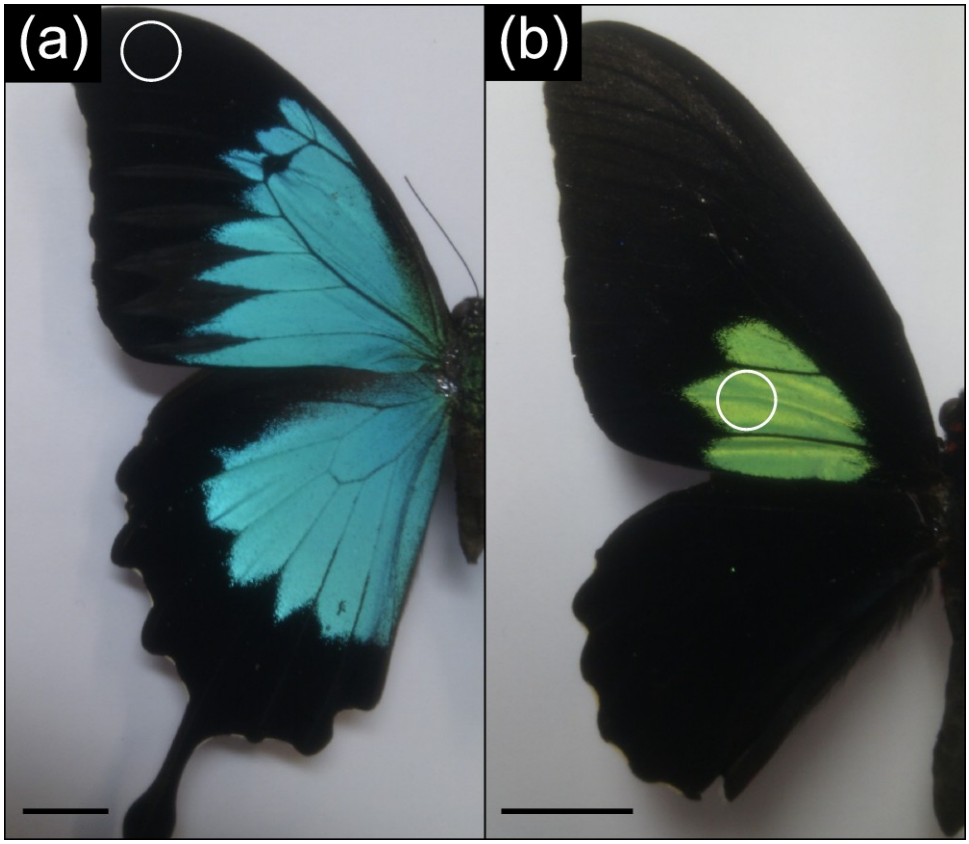

Figure 1. (color on line) Photographs of butterfly species investigated in this study, with the areas from which the scales were taken shown by a white circle in each image: (a) Papilio ulysses, male; (b) Parides sesostris, male. Scale bars are 1 cm.

3 Materials and Methods

The wing scales of two species of Lepidoptera are studied in this work (see Figure 1), chosen as they provide examples of a range of different optical structures. Some structural color features, such as chitin-air multilayers, can only be imaged successfully after careful cross-sectioning. These were avoided in favour of structures located at the scale surface or structures that could easily be revealed by cutting with a razor blade. The two samples studied in this report are as follows:

i. Black dorsal ground scales from *Papilio ulysses* (male) which exhibit an extremely low reflectance, assisted by a complex microstructure designed to scatter and trap light and so enhance absorption (Vukusic 2004).
ii. Dorsal scales from *Parides sesostris* (male) from an area which exhibits a high reflectance of green light (Figure 1c) due to differently-oriented domains of a 3D photonic crystal located beneath the surface structures (Vukusic 2003; Poladian 2009; Saranathan 2010).

3.1 Sample preparation

The Lepidoptera specimens were all purchased in a dead and dry form from The Insect Company, UK (http://www.insectcompany.com). Scales from each specimen were transferred from the wings with tweezers and deposited onto carbon tabs attached to 1 cm diameter aluminium SEM stubs (Agar Scientific, Ltd.). For the *P. sesostris* sample, razor blades were used to cut through some of the scales to reveal the underlying photonic crystal structures beneath the upper lamina. The samples were left overnight to allow the carbon tabs to dry and fully outgas before loading into the helium ion microscope.

3.2 Helium Ion Microscopy

HIM was performed in a Orion Plus™ helium ion microscope (Carl Zeiss). The accelerating voltage was approximately 30 keV and the beam current was between ~0.1 and 2 pA with a 10 µm aperture and a working distance of between 7 and 8 mm. Beam alignment and astigmatism correction was performed on a conductive sample before moving a butterfly scale into position and focusing. The electron flood gun was powered up in line mode and a He beam dwell time of 1 µs was selected. The flood energy, flood time, x deflection and y deflection were then varied iteratively to optimize the contrast of the image. Charge neutralisation was achieved with typical flood times of 1000 µs and flood energies in the range 700-1100 eV. Line averaging of 64 was then implemented to capture the image. On some images, it was necessary to perform post-capture histogram equalization to redistribute the intensity variation across the entire greyscale range. No other digital enhancement techniques were used.

3.3 Photonic crystal structure measurements

Measurement of the periodicity of the photonic crystal structure found in the scale of *P. sesostris* was performed on an image of the structure at a field of view of 2 µm. The sample was tilted in an attempt to view as close as possible along the normal to the (111), hexagonally-arranged plane (although small variations in domain orientation across the image were unavoidable). Values of the period of the structure were measured using line profiles along the three close packed directions of the hexagonal pattern. The period is given as an average of 90 measurements with the standard deviation used as a measure of the variation in period within the imaged region.

Three dimensional renderings of the level set approximations to the photonic crystal structure in *P. sesostris* were performed in MATLAB. The intermaterial dividing surface (IMDS) between chitin and air is define by the gyroid level set as (Michielsen 2008)

$$\sin X \cos Y + \sin Y \cos Z + \cos X \sin Z = t \tag{1}$$

where

$$X = \frac{2\pi x}{a}; Y = \frac{2\pi y}{a}; Z = \frac{2\pi z}{a} \tag{2}$$

The parameter t determines the volume fraction of chitin to air and a is the lattice parameter. MATLAB volume rendering functions were then used to fill in the chitin part of the gyroid on one side of the IMDS and display the structure as a 3D object with simulated lighting.

3.4 Stereoscopy

Stereoscopic imaging has been employed for extracting depth information in SEM since the 1950s and involves the capture of two images of the same area but at different tilt angles (Wells 1960). The images are placed adjacent to one another and then the stereo effect can be visualized either with the aid of a stereoscope or by simply relaxing the eyes, focusing at infinity, and allowing the images to appear to overlap (parallel viewing method (Goldstein, 2003)).

Stereo pairs were generated by adapting the method described in (Goldstein 2003). An image was captured at a particular tilt angle as described in section 3.2. The specimen was then tilted by 6 degrees and the same area was brought back into focus. A second image was then captured to complete the stereo pair. A tilt of 6 degrees was chosen as this produces good stereo effects for the average pair of human eyes at a comfortable reading distance (Goldstein 2003). A scan rotation of 90° was applied so that the tilt axis was vertical with respect to the image. The two images were then cropped, aligned and rescaled if necessary to produce the stereo pair.

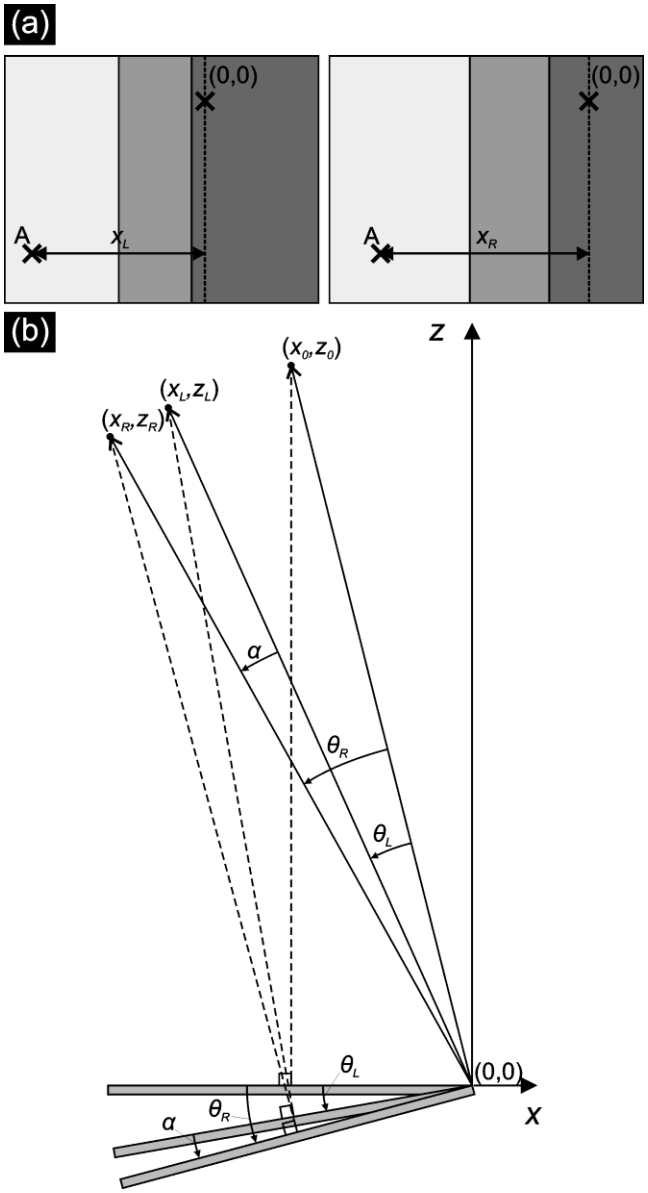

Figure 2. Quantitative stereo analysis schematic diagrams: (a) Representation of a stereo pair with a feature chosen as the origin (0,0) and feature A, on a higher plane compared to the origin, identified on both left and right images; (b) Schematic diagram of sample tilt angles and vectors from the origin to a feature of interest for height calculations performed on stereo pair representation in (a).

Furthermore, this technique can be extended to extract quantitative depth information from HIM images (Boyde 1973). For the following analysis, a parallel projection approximation is used, which is valid at all magnifications greater than about 100, for which the beam deflection angles are sufficiently small (Goldstein 2003). A feature which is visible in both images of the stereo pair is selected as the origin, (0,0) (see Figure 2). Vectors are then drawn from and perpendicular to the y tilt axis passing through the origin to another feature visible on both images in the pair (feature A). The tilting of the stage between capturing the left and right images can be represented as a rotation about the y axis by an angle α, where

$$\alpha = \theta_R - \theta_L \tag{3}$$

and θ_R and θ_L are the stage tilt angles for the left and right images, respectively. The vector joining the tilt axis running through the origin to the feature of interest in the left image, (x_L,z_L), can be transformed to the equivalent vector in the right image, (x_R,z_R), by a rotation anticlockwise of α, with the following rotation matrix:

$$\begin{bmatrix} x_R \\ z_R \end{bmatrix} = \begin{bmatrix} \cos\alpha & -\sin\alpha \\ \sin\alpha & \cos\alpha \end{bmatrix} \begin{bmatrix} x_L \\ z_L \end{bmatrix} \quad (4)$$

The z component of the vector in the left image, z_L, is then given in terms of the x components, x_L and x_R measured from the two images:

$$z_L = \frac{x_L \cos\alpha - x_R}{\sin\alpha} \quad (5)$$

A vector rotation of $-\theta_L$ can now be performed on (x_L,z_L) to calculate (x_0,z_0), which is the vector joining the tilt axis running through the origin to the feature of interest at zero degrees tilt:

$$\begin{bmatrix} x_0 \\ z_0 \end{bmatrix} = \begin{bmatrix} \cos\theta_L & \sin\theta_L \\ -\sin\theta_L & \cos\theta_L \end{bmatrix} \begin{bmatrix} x_L \\ z_L \end{bmatrix} \quad (6)$$

The height difference between the origin and the feature of interest at zero degrees tilt is then given by:

$$\begin{aligned} z_0 &= z_L \cos\theta_L - x_L \sin\theta_L \\ &= \left(\frac{x_L \cos\alpha - x_R}{\sin\alpha} \right) \cos\theta_L - x_L \sin\theta_L \end{aligned} \quad (7)$$

3.5 VP SEM

To provide a comparison, the *P. ulysses* sample was also imaged in a EVO™ LS25 environmental SEM (Carl Zeiss), with a LaB_6 source and a VP detector, operated in variable pressure (VP) mode at a pressure of 13 Pa (adjusted to achieve optimum charge neutralization). The accelerating voltage was 25 kV, the beam current was 707 pA and the working distance was 6 mm.

To quantitatively compare images obtained from HIM and VP-SEM, line profiles of the contrast changes across edges of the structures imaged were extracted. A linear fit was performed on the region of the line profile representing the edge and then the distance over which the contrast changes from 25% to 75% of its overall change was measured to provide a figure of merit for image sharpness. Five line profiles, each averaged over 20 pixels, were extracted from each image and an average of the resulting sharpness value was calculated, along with the standard deviation as a value of the uncertainty in the result.

4 Results and Discussion

4.1 Black ground scales from *Papilio ulysses*

HIM images of the black ground scale from *Papilio ulysses* over a range of magnifications and tilt angles are presented in Figure 3. The scale is typical of the ground scales found on most papilionids and is a variation on the general structure of ground scales found throughout the lepidopteran families (Ghiradella 1985). Such scales have been described in detail by Ghiradella *et al.*, who introduced terminology for the typical features present (Ghiradella

1989; Ghiradella 1991). This terminology is used in the annotated sketch in Figure 3d to identify the features in the accompanying HIM image (Figure 3c). The scales are projections from single epidermal cells on the surface of the wing (Vukusic 2001; Ghiradella 1991). The cell extends out from the wing, lays down cuticle material and then dies back allowing the cuticle to dry and harden (Ghiradella 1991). The complex structure of the final scale is thought to develop through a combination of direct cellular membrane control and via the exploitation of elastic buckling under stress (Ghiradella 1994). The fully developed scale consists of a flat and relatively featureless lower lamina separated from an intricately-structured upper lamina, by curved pillars called trabeculae, forming a cavernous scale interior. The upper lamina consists of a series of parallel ridges running longitudinally along the scale with a separation of 2-3 µm. Extending between the ridges are networks of cross-ribs defining a mesh of irregular windows into the hollow interior. These are a variation of the regular rows of windows defined by straight cross-ribs that is more typical of ground scales in Lepidoptera (Ghiradella 1985). Thin lamellae lie on the tops of the ridges, slanted towards the wide end of the scale, with some overlap. In other species (e.g. those of the *Morpho* family (Kinoshita 2002)), these lamella are further developed and overlapped to form optically active multilayer structures, leading to vivid and iridescent coloration, but this is not the case in *P. ulysses*, where lamella overlap is minimal. Fine microribs run down the ridge walls from the lamellae to and across the cross-ribs.

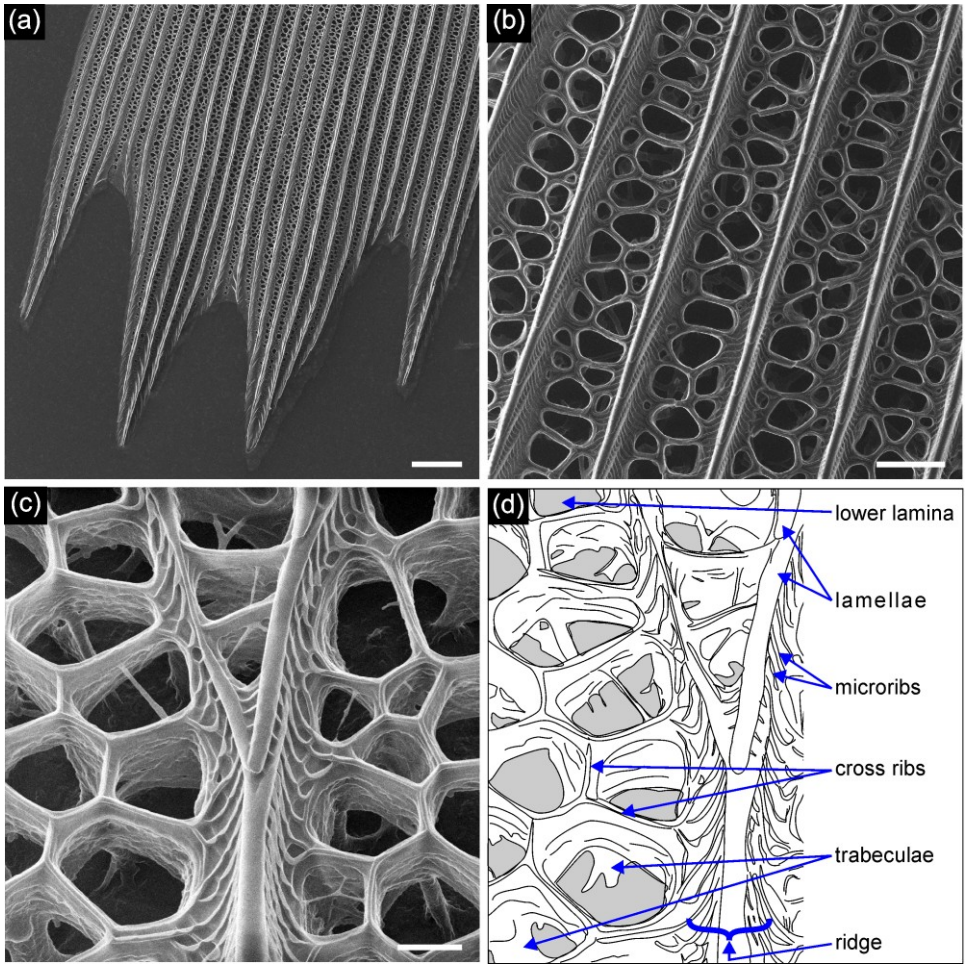

Figure 3. (a-c) HIM images of P. ulysses black ground scale at various magnifications and tilt angles: (a) 10 µm scale bar, 0° tilt; (b) 2 µm scale bar, 0° tilt; (c) 400 nm scale bar, 21° tilt (d) annotated sketch of HIM image in (c), identifying features on the wing scale using nomenclature from the work of Ghiradella (Ghiradella 1989; Ghiradella 1985) .

The elaborate structure of the *P. ulysses* ground scale shown Figure 3 makes it a highly efficient light absorber and hence leads to the extreme blackness of the areas of the wings covered with these scales. Melanin pigment is responsible for absorbing light but the structure on the wing is thought to act in several ways to enhance light absorption (Vukusic 2004):

i) The structure increases the surface area of the wing and so increases the amount of pigment exposed to incident light.
ii) The structure scatters incident light, guiding it into the hollow interior of the scale and increasing the optical path length of light through pigment-containing parts of the scale.
iii) The tapering of the cross-ribs and the presence of subwavelength-scale microribs has an antireflective effect, through a graded index mechanism similar to that of the nipple arrays found on the eyes and wings of some species of moth (Bernhard 1967).

Vukusic *et al.* demonstrated the importance of the structure to the absorbing efficiency of the scale by removing its effect using an index matching fluid, which resulted in a ~40% decrease in optical absorption. The development of such a highly-absorbing structure could have been driven by the need for thermoregulation (as a way of increasing wing and body temperature (Biró 2003)) and/or to enhance the vividness of the blue areas of the wing (see Figure 1), both by providing a highly-contrasting border and by reducing back reflection of light transmitted through the multilayered reflector on the cover scales.

Similar areas of black scales from *Papilio ulysses* were imaged directly from above (zero tilt) using HIM and VP SEM to compare the two techniques. From Figure 4, the resolution and depth-of-field limitations of VP-SEM are immediately apparent in comparison with the HIM technique. In the HIM images (Figure 4 b & d), the entire sample appears in focus and fine surface details are visible where as this is not the case in the corresponding VP-SEM images (a & c). The large depth-of-field in HIM (5-10 times that of an SEM) is a result of the atomic scale source size which allows the microscope column optics to be run with a smaller demagnification than in a typical SEM. Consequently, the beam convergence angle, γ, is smaller allowing sharp imaging of features at a wider range of working distances within one image. This is particularly useful for structural color investigation where, as the images presented here clearly show, the features of interest extend well into the third dimension. Measurements of the contrast change (line profile) across edges of the features of the scale give a quantitative assessment of the sharpness of the image. These measurements (Figure 4 e & f) reveal a factor of ~16 difference between the two techniques, with the edge sharpness of the HIM image measured as 3.4 nm +/- 0.5 nm, compared to 55.3 nm +/- 8.4 nm for the VP-SEM image.

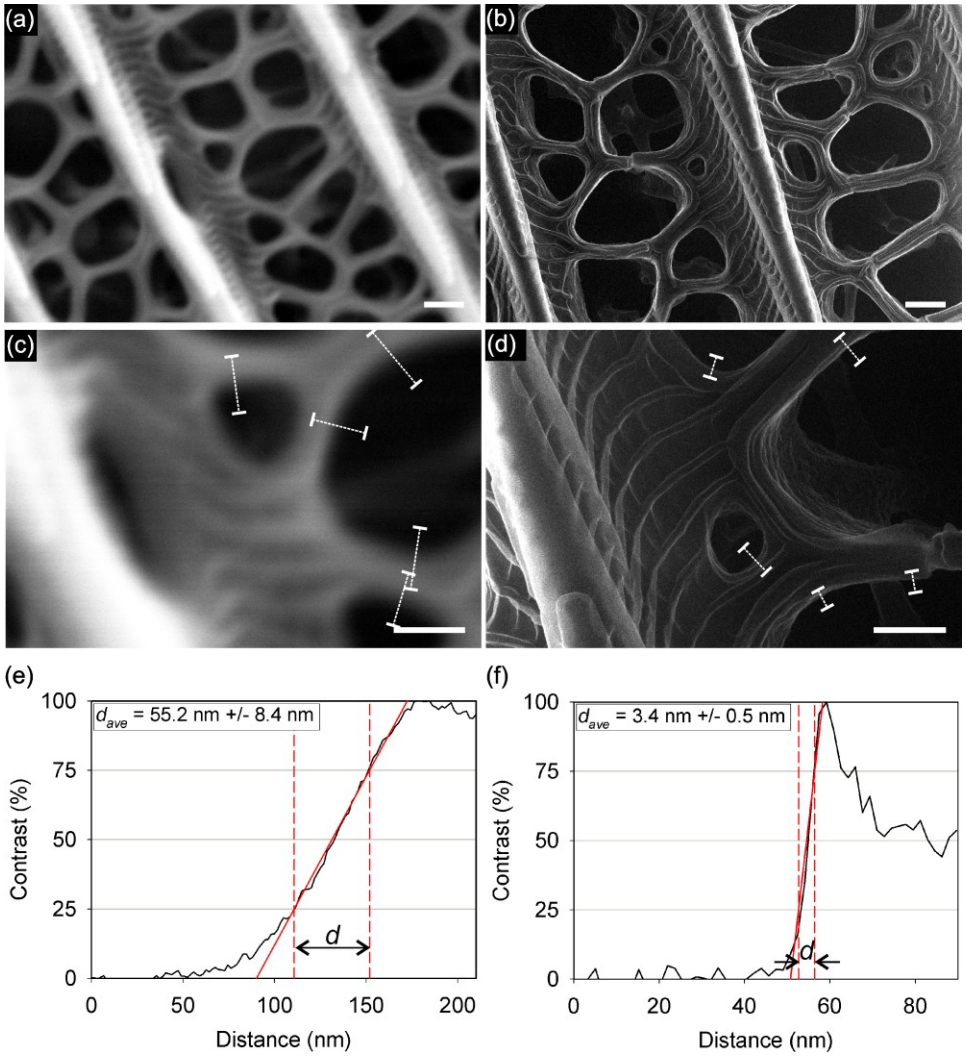

Figure 4. (a-d) Images of uncoated Papilio ulysses black dorsal scales taken at two different magnifications at zero tilt angle (a & c) EVO SEM in VP Mode; (b & d) Orion HIM. Scale bars: (a & b) 500 nm, (c & d) 300 nm; (c) and (d) also show edges across which line profiles were measured for the calculation of image sharpness; (e & f) Examples of line profiles on (e) EVO image, (f) Orion image, with the image sharpness, dave, given as an average of 5 measurements.

The features of the *P. ulysses* ground scale described above can also be resolved in SEM images of coated specimens. However, the fine surface detail visible on the inside walls of the cross-ribs and trabecula in Figure 3c would be difficult to resolve in SEM and could easily be obscured by a conductive coating. This fine texture on the surface could be evidence of chitin bundles or fibrils (Vukusic 2001; Ghiradella 1994; Neville 1976) which appear to be oriented predominately horizontal with respect to the scale surface. Indeed, a number of thin fibrils (~10-30 nm in diameter) can be observed extending across the windows in the cross-ribbed structure, providing further evidence of the fibrillous nature of the cuticle material. Future work will include imaging at even higher magnifications in an attempt to resolve yet finer details, with care taken to avoid damaging the material with high beam doses. The ability to resolve such details could prove important in understanding the growth mechanisms that produce these structures and could uncover hitherto unknown differences between species/families at this fine structural level. It may also help to provide further insights into the evolution of these optical effects.

4.2 Green cover scales from *Parides sesostris*

The green cover scale from the second papilionid included in this study, *P. sesostris*, also has an upper lamina consisting of an array of ridges running longitudinal along the scale, with a periodicity of ~0.6-1 µm (Figure 5a). The cross-ribs in this scale are straighter and define more regular-shaped windows into the scale interior (Figure 5a, inset) compared to the mesh-like inter-ridge structure found on *P. ulysses* ground scales. The lamellae on top of the

ridges are not individually discernable but appear to have formed into continuous bands. Microribs are again present running down the ridge to the cross-ribs. However, perhaps the most striking feature of this scale is the lattice structure located underneath the top lamina, in the interior of the scale. The images in Figure 5 show this structure exposed at the corner of the scale where a section of the upper lamina has been removed. The structure consists of arrays of air holes in a chitin matrix and is an example of a three-dimensional biological photonic crystal that has been studied in detail by a number of different groups (Vukusic 2001; Michielsen 2008; Poladian 2009; Saranathan 2010; Ghiradella 1994). Figure 5 shows that the structure is divided into domains or crystallites, at different orientations but within which the arrangement of holes appears regular and ordered. Between domains, areas of disorder exist, similar to grain boundaries in a polycrystalline material. Similar structures are found in a number of other species including the papilionid *Teinopalpus imperialis* and the lycaendids *Callophrys rubi* and *Cyanophrys remus* (Michielsen 2008; Saranathan 2010). Higher magnification images of the area of the photonic crystal shown within the dashed box in Figure 5 are presented in Figure 6. This particular domain is at an orientation with respect to the viewing direction that leads to the observation of a hexagonal array of holes. The large depth-of-field available with HIM allows the edges of the holes in the several layers beneath the surface to be discerned which gives information on small variations in the orientation with one domain. The period of the structure in the domain shown in Figure 6 was measured to be 223 nm +/- 17nm. This is within the range reported by Michielsen and Stavenga of 260 +/- 63 nm, based on a TEM study (Michielsen 2008).

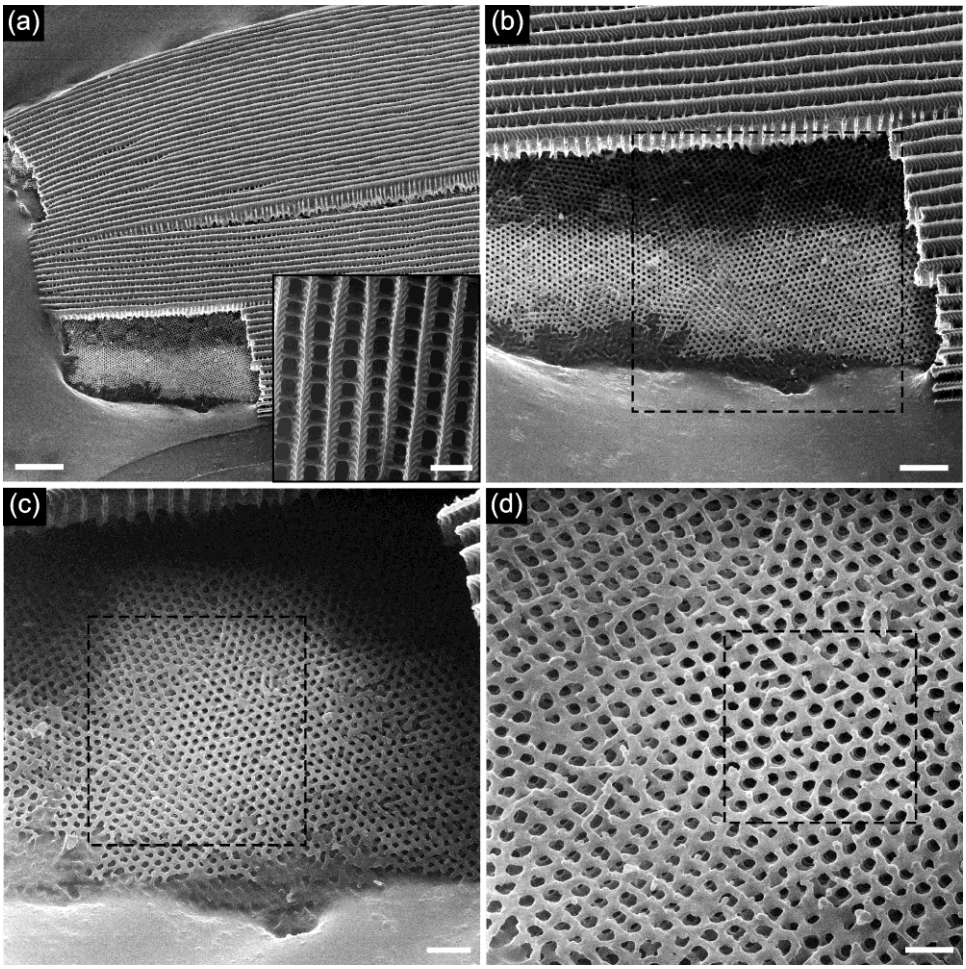

Figure 5. HIM SE images of a region of a green scale from Parides sesostris: (a) Low magnification image showing the end of a scale with a section of the upper lamina removed to reveal the underlying photonic crystal structure; (b), (c) & (d) are successive zooms on the area in which the upper lamina has been removed. The black dashed boxes mark the area imaged at higher magnification in the subsequent image. Scale bars and stage tilt angles: (a) 5 µm, 30°, (inset) 1 µm, 0°; (b) 2 µm, 30°; (c) 1 µm, 35°; (d) 1 µm, 40°.

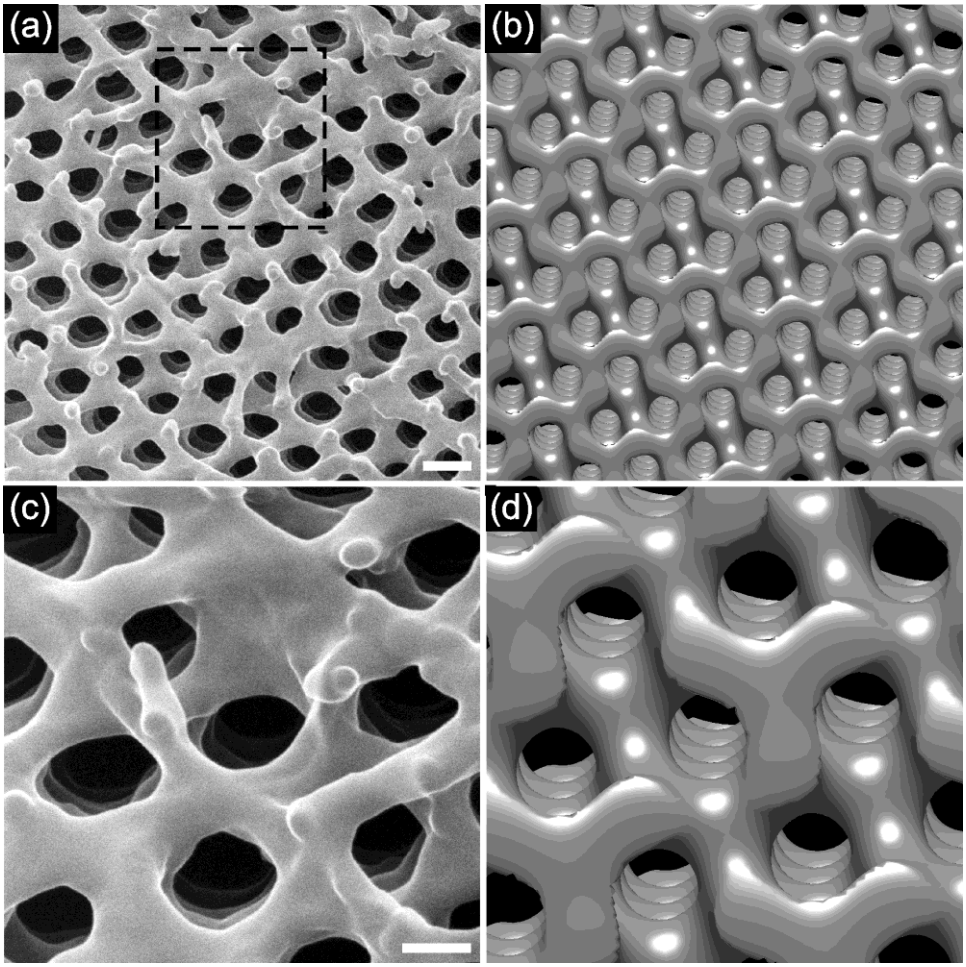

Figure 6. (a, c) High magnification HIM SE images of 3D photonic crystal found in the Parides sesostris wing scale. (a) is a zoom on the area marked by the box in Figure 5(d), and the box in (a) marks the area for the image in (c). (b,d) 3D renderings of air-chitin gyroid structure, sliced at arbitrary position along the (111) plane and oriented to approximately match the viewing angle of the structures in the corresponding HIM images in (a) and (c) . Scale bars and stage tilt angles: (a) 200 nm, 40°; (b) 100 nm, 45°.

Various crystal geometries have been proposed for the structure found within each domain including face-centred cubic (Ghiradella 1994) and tetrahedral (Vukusic 2001) but the latest understanding, first suggested by Michielsen and Stavenga is that the structure more accurately matches that of the bicontinuous, triply periodic gyroid structure (Michielsen 2008; Saranathan 2010). In this type of structure, two distinct and continuous volumes separated by an intermaterial dividing surface (IMDS) form a complex interlocking 3D network. Such structures are known to form through self-assembly of lipid bilayers as a way to minimize curvature energy. Saranathan *et al.* developed this idea into a model for the development of such a structure in wing scale cells (Saranathan 2010). This first involves the formation of a pentacontinuous, core-shell double gyroid structure from the interaction of the cell plasma membrane and the smooth endoplasmic reticulum. Chitin is then deposited into the extracellular space that forms the core of one of the gyroid networks enclosed by the plasma membrane lipid bilayer. The cell then dies away and air replaces the cytoplasm and membranes, leaving the air-chitin bicontinuous gyroid structure. The classification of the *Parides sesostris* photonic crystal as a gyroid has been supported by evidence from small angle x-ray scattering (SAXS)(Saranathan 2010), pattern matching in TEM cross-sections (Michielsen 2008) and photonic band structure calculations (Poladian, 2009). The IMDS of the gyroid structure can be approximated by constant mean curvature surfaces which themselves can be modelled by level set approximations (Saranathan 2010; Michielsen 2008; Wohlgemuth 2001). Three dimensional renderings of the level set approximations in MATLAB, sliced, scaled and oriented normal to the (111) direction to match the corresponding HIM images in Figure 6 (a & c) are presented in Figure 6 (b & d). The models were constructed using a lattice parameter of 223 nm (taken from measurement described above on the domain imaged in Figure 6) and a chitin volume fraction of 0.4 (t =-0.3 in equation 1) (Michielsen 2008). The simulated structures match well to the imaged section of the photonic crystal and the

analysis suggests that it is possible to determine the orientation of domains by orienting the model to match the edges of the holes in the underlying layers, viewed through the top layer holes in the HIM image. In principle, this technique could be used to characterize the orientation of the different domains within the scale and the smaller changes in orientation within one domain but this is left as an area for future work.

Also worth noting is the smooth appearance of the surface of the photonic crystal structure, even at the high magnification used for capturing the image in Figure 6c. This contrasts with the nanoscale texturing observed on the inner walls of the windows in the of the upper lamina structures of both this scale and the *P. ulysses* ground scale and could provide clues to differences in the way cuticle is formed in these areas.

The *P. sesostris* wing scale studied here reflects green light as a result of the photonic band gap exhibited by the periodic structure underneath the top lamina. Band gap calculations indicate that gyroid structured photonic crystals made from materials with relatively low refractive index contrast (e.g. ~1.5 between chitin and air) do not exhibit complete photonic band gaps and so reflectance is highly angle dependent for a structure with a single orientation (i.e. the structure should exhibit iridescence). The reflectance characteristics of the *P. sesostris* wing scale however show little variation with viewing angle. A combination of mechanisms is thought to be responsible for the suppression of iridescence:

i) The division of the structure into domains at different orientations prevents strong deviations in reflected intensity for the structure as a whole and so suppresses iridescence (Vukusic 2001).
ii) The structure of the upper lamina acts to either collimate the incident light, reducing the range of angles it is incident at, or to randomize the incident and reflected light (Poladian 2009).

The tubular nature of the windows into the interior of the scale formed by the ridges and cross ribs of the upper lamina is evident from the cross-sectional images in Figure 7. The depth-of-field in the images shows both ridge and photonic crystal structures in focus. Trabeculae linking the two are also visible in Figure 7b.

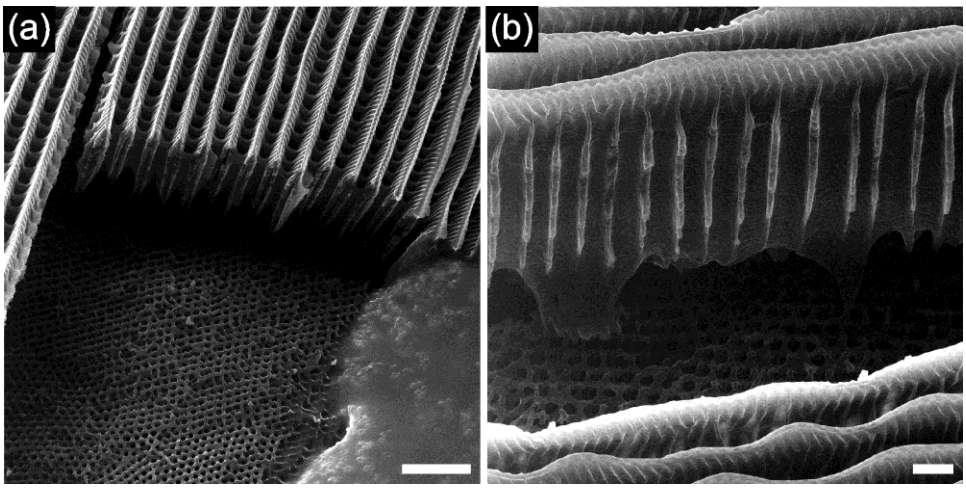

Figure 7. HIM SE images of the green scale from Parides sesostris showing detail of ridges and cross-ribs in cross-section on the upper lamina from two different viewpoints. Scale bars and stage tilt angles: (a) 2 µm, 40°; (b) 500 nm, 45°.

It has been suggested that the non-iridescent reflection of green light could be a camouflaging mechanism as it resembles the diffuse green coloration of leaves (Vukusic 2001; Ghiradella 1991). However, as Figure 1b clear illustrates, only part of the wing exhibits this coloration and the remaining black areas would seem to be rather conspicuous against a green background in daylight. More likely is the suggestion that the coloration could be used in courtship displays as a method for the female to recognize potential mates (Ghiradella 1991) or for cryptic signalling using reflection of circularly polarized light in the UV (Poladian 2009).

4.3 Stereo Pairs

As seen in the previous sections, the large depth-of-field available in HIM can be used in combination with sample tilt to gain insights into how the features on lepidoteran wing scales lie with respect to one another in the 3rd dimension. Figure 8 presents a series of images from the same region of the ground scale of *Papilio ulysses* taken at various tilt angles. The large depth-of-field means that all parts of the sample remain in focus as the sample is tilted and the features on the side walls and lower lamina are revealed. This can be exploited further by forming stereo pairs from images taken at two tilt angles. Figure 9a is a stereo pair formed from images taken at stage tilts of 15° and 21° (i.e. images (d) and (e) from Figure 8) and when viewed using the parallel viewing technique (Goldstein 2003), provides a feel for the depth of the crevices between the cross-ribs and the height of the ridge and lamellae. Likewise, the 3D nature of the photonic crystal structure from *Parides sesostris* is apparent from the stereo pair in Figure 9. (These stereo images can also be viewed through filtered spectacles in the form of red-cyan anaglyphs included in the supplementary material section (Figures S1 and S2)).

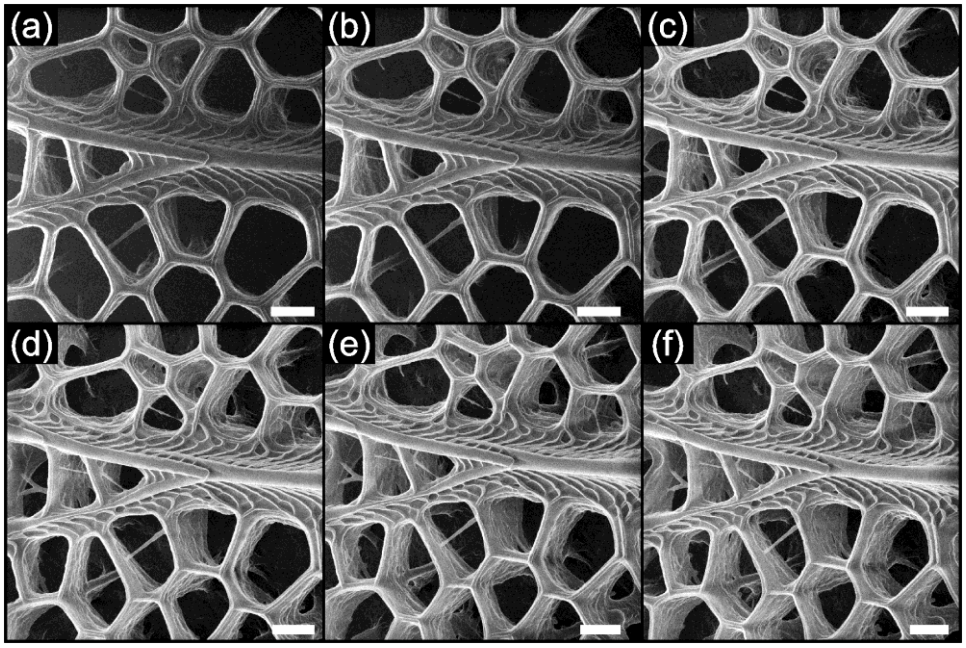

Figure 8. HIM SE image tilt series from the same area of the black Papilio ulysses ground scales. Stage tilt angles: (a) 0°, (b) 5°, (c) 10°, (d) 15°, (e) 21°, (f) 26°. All scale bars are 400 nm.

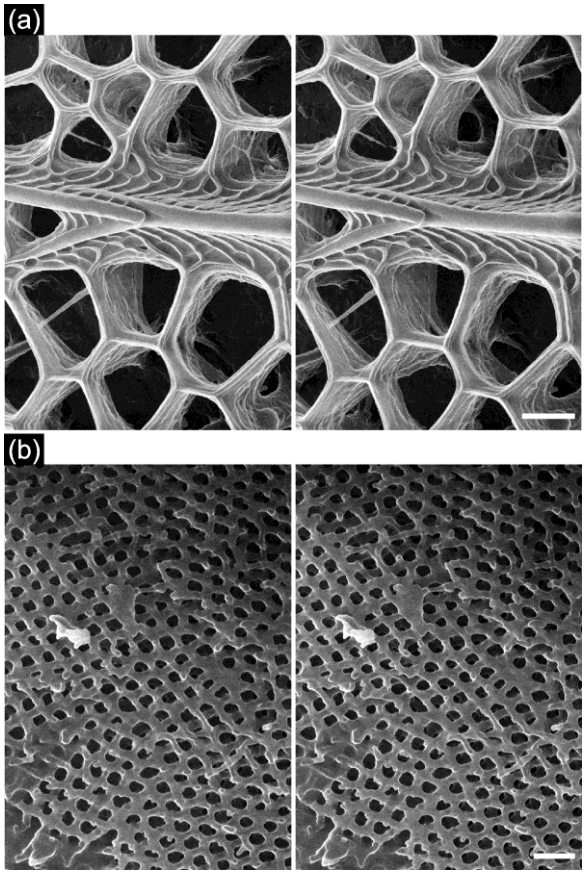

Figure 9. (a) HIM SE stereo pairs consisting of images of (a) region of black cover scale from P. ulysses and (b) photonic crystal structure from P. sesostris. Scale bars (which apply to both images in the pair) and stage tilt angles: (a) 200 nm, left 15°, right 21°, (b) 500 nm, left 0°, right 6°.

As a demonstration of quantitative feature height determination from HIM stereo pairs, a stereo pair of images from the ground scale of *P. ulysses* was generated (Figure 10) and a feature on the lower lamina surface was chosen as the origin (0,0). The calculated height differences between the origin and feature A, at the edge of the cross-ribs, and feature B, on top of the lamella at the peak of the ridge are given in Table 1. As a comparison, measurements were performed on a cross-sectional TEM micrograph of a wing scale from the same species from the literature (Vukusic 2004). The distances from the lower lamina inner surface to features at the equivalent positions to A and B were measured across the TEM micrograph and are included in Table 1. The HIM height measurements are within the range of the measurements for equivalent points on the TEM micrograph which validates the HIM technique. Further measurements are required on samples of known dimensions to assess the accuracy of this measurement technique, which will ultimately be limited by the accuracy of the tilt stage. Nevertheless, the preliminary study reported here shows that the technique gives values that are similar to measurements from TEM cross-sections, with the benefit that time-consuming TEM sample preparation is avoided.

Feature	z_{0HIM}(µm)	z_{0TEM}(µm)
A	1.5	1.1-1.6
B	1.9	1.9-2.6

Table 1. Results from analysis of the distances in the z direction from the inner surface of the lower lamina to the edge of the cross-ribs (feature A) and to the top of the ridge (feature B). z_{0HIM} is the distance calculated from the HIM stereo pairs in Figure 10. z_{0TEM} is the range measured from the TEM cross-section micrograph from (Peter Vukusic et al. 2004).

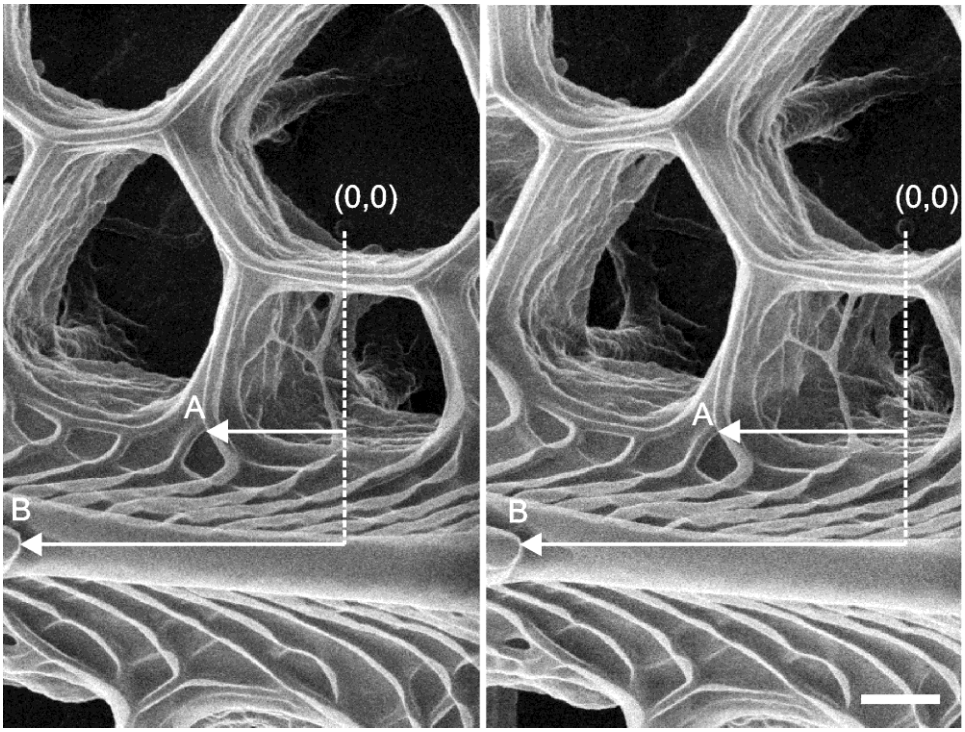

Figure 10. (a) Stereo pair of images from the ground scale of Papilio ulysses, taken at a stage tilts of 10° (L) and 15°(R), with a feature is chosen as the origin (0,0) and two features, A and B, identified for height calculations. Scale bar (which applies to both images in the pair) is 200 nm.

Stereo pair generation, with quantitative feature height measurements can be performed in SEM but the larger depth-of-field available with HIM leads to a better stereo effect because the viewer can focus on features in both the foreground and background. In addition, height measurements are made more accurate because the sharpness of both the foreground and background features allows their precise location on the images to be identified. Therefore, compared to SEM, the difference in the position of these features in the left and right images of the stereo pair can be more accurately defined, and this applies to features separated by greater distances in the z direction. Software exists (e.g. Mex™ from Alicona) that extends this concept of feature height extraction from stereo pairs to the construction of a three-dimensional elevation profiles. This has been successfully applied to biological samples in SEM (Tomes 2007; Chen 2010; Akisaka 2008) and future work could involve applying this to HIM-generated stereo pairs to create three-dimensional topography maps.

5 Conclusions

The high resolution and large depth-of-field capabilities of HIM have been exploited to capture images of the microstructure of scales from the wings of two species of butterfly to a level of detail not previously obtained with SEM. Conductive coating is not required because effective charge neutralization can be achieved using an electron flood gun integrated into the HIM. Fine texturing on the inner walls of the cross-ribs on the upper lamina of *P. ulysses* scales was identified as possible evidence of the fibrillous nature of the cuticle material forming these structures. The photonic crystal structure found in the interior of *P. sesostris* scales matched well to 3D renderings of a bicontinuous air-chitin gyroid structure. In addition, the visibility of the underlying hole edges could be used to orientate the rendered model and so characterize both the rough orientation of a particular domain and possibly the small variations in intra-domain orientation. Stereo pairs were generated to provide insight into the three-dimensionality of the structures and quantitative height information extracted from pairs of images matched well to measurements on a TEM cross-sectional micrograph from the literature. The large depth-of-field available in HIM proved particularly valuable for this as it allowed surfaces with height differences of several micrometers to be

imaged in focus, simultaneously, at high magnifications (e.g. a 3 µm field-of-view). Furthermore, the simple sample preparation requirements of SEM were retained.

This study has demonstrated the potential of this new type of microscopy for imaging biological features responsible for structural color effects to a high level of detail. There are a vast number of other such structures in nature and it is hoped that HIM characterization can be employed to provide a deeper understanding of the mechanisms at play in the development and operation of these remarkable natural structures.

6 Supplementary Material

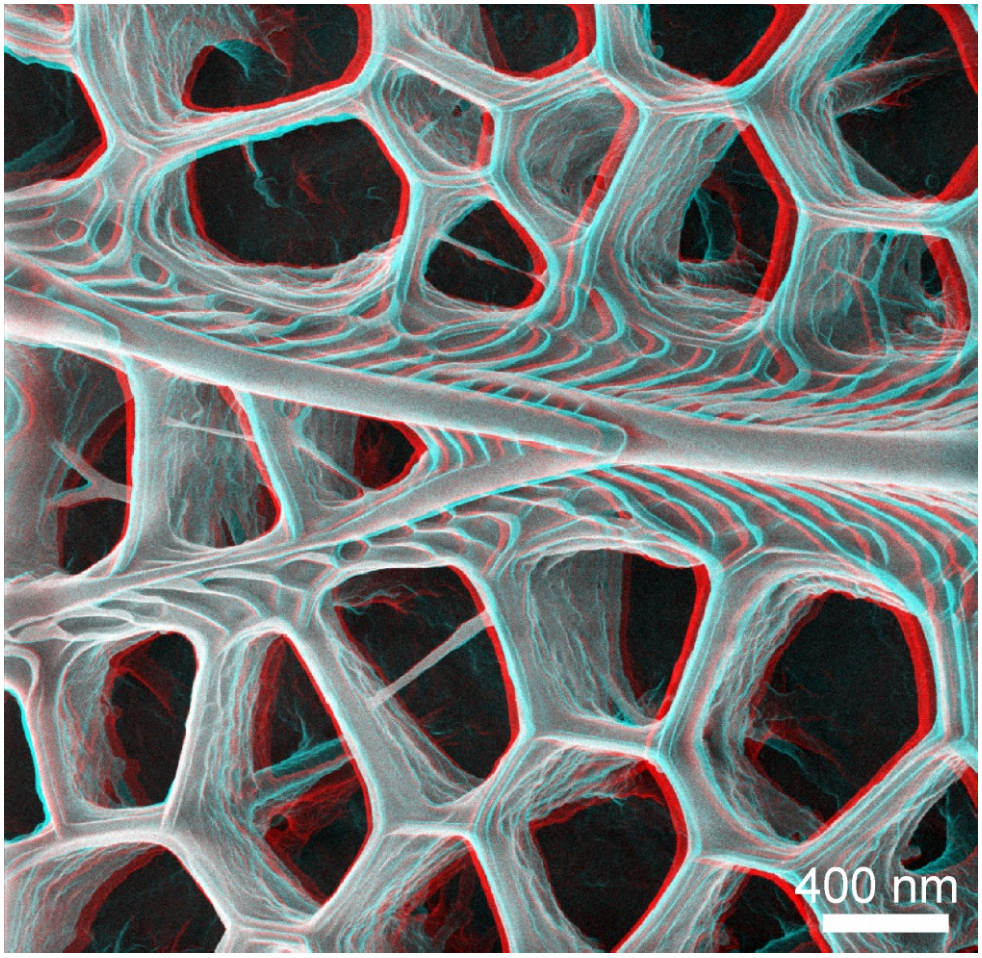

Figure S1. 3D anaglyph of *P. ulysses* black ground scale for viewing through red/cyan filtered spectacles.

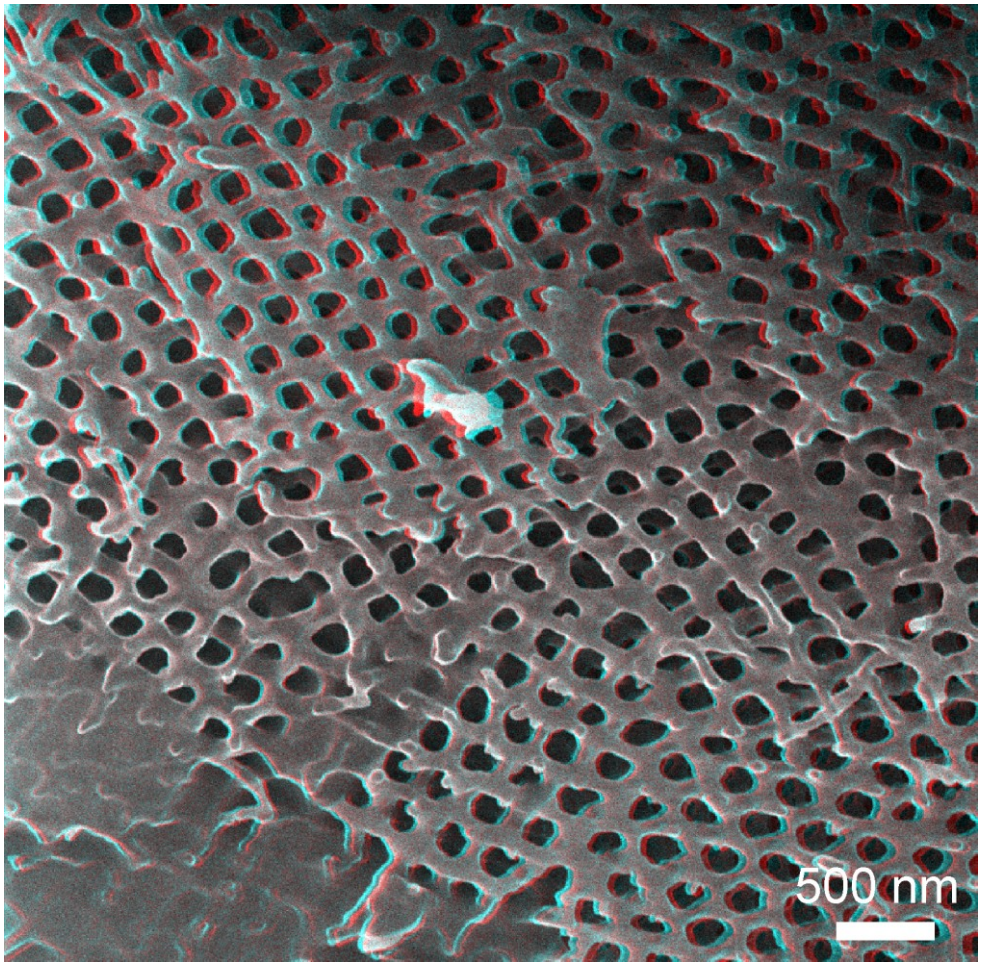

Figure S2. 3D anaglyph of *P. sesostris* green scale photonic crystal for viewing through red/cyan filtered spectacles.

7 References

Akisaka T, Yoshida H, Suzuki R, Takama K. (2008). Adhesion structures and their cytoskeleton-membrane interactions at podosomes of osteoclasts in culture. Cell and Tissue Research, 331(3), 625-41.

Argyros A, Manos S, Large MCJ, McKenzie DR, Cox GC, Dwarte DM. (2002). Electron tomography and computer visualisation of a three-dimensional “photonic” crystal in a butterfly wing-scale. Micron, 33(5), 483-487

Bazou D, Behan G, Reid C, Boland JJ, Zhang HZ. (2011). Imaging of human colon cancer cells using He-Ion scanning microscopy. Journal of Microscopy, 242(3) 290-294.

Bernhard CG. (1967). Structural and functional adaption in a visual system. Endeavour, 26, 79-84.

Berthier, S., Boulenguez, J., & Bálint, Z. (2006). Multiscaled polarization effects in Suneve coronata (Lepidoptera) and other insects: application to anti-counterfeiting of banknotes. Applied Physics A, 86(1), 123-130.

Biró LP, Bálint Z, Kertész K, Vértesy Z, Márk G, Horváth Z, Balázs J, Méhn D, Kiricsi I, Lousse V, Vigneron JP. (2003). Role of photonic-crystal-type structures in the thermal regulation of a Lycaenid butterfly sister species pair. Physical Review E, 67(2), 1-7.

Boden SA, Bagnall DM. (2008). Tunable reflection minima of nanostructured antireflective surfaces. Applied Physics Letters, 93(13), 133108.

Boden SA, Bagnall DM. (2010). Optimization of moth-eye antireflection schemes for silicon solar cells. Progress in Photovoltaics: Research and Applications, 18(3), 195-203.

Boyde A. (1973). Quantitative photogrammetric analysis and qualitative stereoscopic analysis of SEM images. Journal of Microscopy, 98, 452-471.

Bálint Z, Vértesy Z, Kertész K, Biró LP. (2004). Scanning Electron Microscopic Investigations in Butterfly Wings : Detecting Scale Micro- and Nanomorphology and Understanding their Functions. Current Issues on Multidisciplinary Microscopy Research and Education, 87-92.

Chen X, Ostadi H, Jiang K. (2010). Three-dimensional surface reconstruction of diatomaceous frustules. Analytical Biochemistry, 403(1-2), 63-6.

Chen Y, Centonze VE, Verkhovsky A, Borisy GG. (1995). Imaging of cytoskeletal elements by low-temperature high-resolution scanning electron microscopy. Journal of Microscopy, 179, 67.

Ghiradella H. (1985). Structure and Development of Iridescent Lepidopteran Scales: The Papilionidae as a Showcase Family. Annals of the Entomogical Society of America, L78(2), 252-264.

Ghiradella H. (1989). Structure and Development of Iridescent Butterfly Scales: Lattices and Laminae. Journal of Morphology, 202, 69-88.

Ghiradella H. (1991). Light and color on the wing: structural colors in butterflies and moths. Applied Optics, 30(24), 3492–3500.

Ghiradella H. (1994). Structure of butterfly scales: patterning in an insect cuticle. Microscopy Research and Technique, 27(5), 429-38.

Gilmore IS, Seah MP. (2003). Investigating the difficulty of eliminating flood gun damage in TOF-SIMS. Applied Surface Science, 203-204, 600-604.

Goldstein JI, Newbury DE, Joy DC, Lyman CE, Echlin P, Lifshin E, Sawyer L, Michael JR. (2003). Scanning Electron Microscopy and X-ray Microanalysis. In Scanning Electron Microscopy and X-ray Microanalysis (3rd ed., pp. 213-215). New York: Springer Science + Business Media, Inc.

Goldstein JI, Newbury DE, Joy DC, Lyman CE, Echlin P, Lifshin E, Sawyer L, Michael JR. (2003). Chapter 15. Procedures for Elimination of Charging in Nonconducting Specimens. In Scanning Electron Microscopy and X-ray Microanalysis (3rd ed., p. 672). New York: Springer Science + Business Media, Inc.

Huchital D, McKeon R. (1972). Use of an Electron Flood Gun to Reduce Surface Charging in X-Ray Photoelectron Spectroscopy. Applied Physics Letters, 20(4), 158-159.

Kinoshita S, Yoshioka S. (2005). Structural colors in nature: the role of regularity and irregularity in the structure. ChemPhysChem, 6(8), 1442-59.

Kinoshita S, Yoshioka S, Kawagoe K. (2002). Mechanisms of structural colour in the Morpho butterfly: cooperation of regularity and irregularity in an iridescent scale. Proceedings of the Royal Society of London B, 269(1499), 1417-21.

Kurachi M, Takaku Y, Komiya Y, Hariyama T. (2002). The origin of extensive colour polymorphism in Plateumaris sericea (Chrysomelidae, Coleoptera). Naturwissenschaften, 89(7), 295-298.

Michielsen K, Stavenga DG. (2008). Gyroid cuticular structures in butterfly wing scales: biological photonic crystals. Journal of the Royal Society, Interface, 5(18), 85-94.

Neville AC, Parry DA, Woodhead-Galloway J. (1976). The chitin crystallite in arthropod cuticle. Journal of Cell Science, 21(1), 73-82.

Parker AR. (2000). 515 million years of structural colour. Journal of Optics A: Pure and Applied Optics, 2, R15.

Parker AR, Townley HE (2007). Biomimetics of photonic nanostructures. Nature Nanotechnology, 2(6), 347-53.

Parker A, McKenzie D, Large MCJ. (1998). Multilayer reflectors in animals using green and gold beetles as contrasting examples. Journal of Experimental Biology, 201(9), 1307–1313

Phifer D, Tuma L, Vystavel T, Wandrol P, Young R. (2009). Improving SEM Imaging Performance Using Beam Deceleration. Microscopy Today, 17(04), 40–49

Poladian L, Wickham S, Lee K, Large MCJ. (2009). Iridescence from photonic crystals and its suppression in butterfly scales. Journal of the Royal Society, Interface, 6 Suppl 2(November 2008), S233-42.

Postek MT. (2006). An approach to the reduction of hydrocarbon contamination in the scanning electron microscope. Scanning, 18(4), 269-274.

Prum RO, Torres R. (2003). Structural colouration of avian skin: convergent evolution of coherently scattering dermal collagen arrays. Journal of Experimental Biology, 206(14), 2409-2429.

Prum, RO, Torres R, Kovach C, Williamson S, Goodman S. (1999). Coherent light scattering by nanostructured collagen arrays in the caruncles of the malagasy asities (Eurylaimidae: aves). Journal of Experimental Biology, 202 Pt 24, 3507-22.

Robinson, VNE. (1974). A wet stage modification to a scanning electron microscope. In JV Sanders & DJ Goodchild (Eds.), Proceedings of the 8th International Congress on Electron Microscopy (pp. 50-51). Canberra, Australia: Australia Academy of Sciences.

Saranathan V, Osuji CO, Mochrie, SGJ, Noh H, Narayanan S, Sandy A, Dufresne, ER, Prum, RO. (2010). Structure, function, and self-assembly of single network gyroid (I4132) photonic crystals in butterfly wing scales. Proceedings of the National Academy of Sciences, 107(26), 11676.

Schatten H. (2011). Low voltage high-resolution SEM (LVHRSEM) for biological structural and molecular analysis. Micron, 42(2), 175-85.

Scipioni L, Stern LA, Notte JA, Griffin B. (2008). Applications Developments with the Helium Ion Microscope. Proceedings of the 2008 NSTI Nanotechnology Conference (pp. 871-874).

Seago AE, Brady P, Vigneron JP, Schultz TD. (2009). Gold bugs and beyond: a review of iridescence and structural colour mechanisms in beetles (Coleoptera). Journal of the Royal Society, Interface, 6 Suppl 2(October 2008), S165-84.

Shevtsova E, Hansson C, Janzen DH, Kjærandsen J. (2011). Stable structural color patterns displayed on transparent insect wings. Proceedings of the National Academy of Sciences of the United States of America.

Stavenga DG, Stowe S, Siebke K, Zeil J, Arikawa K. (2004). Butterfly wing colours: scale beads make white pierid wings brighter. Proceedings of the Royal Society of London B, 271(1548), 1577-84.

Stoddart PR, Cadusch PJ, Boyce TM, Erasmus RM, Comins JD. (2006). Optical properties of chitin: surface-enhanced Raman scattering substrates based on antireflection structures on cicada wings. Nanotechnology, 17(3), 680-686.

Tomes C, Jones JT, Carr CM, Jones D. (2007). Three-dimensional imaging and analysis of the surface of hair fibres using scanning electron microscopy. International Journal of Cosmetic Science, 29(4), 293-9.

Utlaut M. (2007). Chapter 10. Micro-machining and mask-repair. In N. Yao (Ed.), Focused Ion Beam Systems: Basics and Applications (1st ed., pp. 281-282). Cambridge, UK: Cambridge University Press.

Vigneron J, Rassart M, Vandenbem C, Lousse V, Deparis O, Biró LP, Dedouaire D, Cornet A, Defrance P. (2006). Spectral filtering of visible light by the cuticle of metallic woodboring beetles and microfabrication of a matching bioinspired material. Physical Review E, 73(4), 1-8.

Vukusic P, Sambles R. (2001). Shedding light on butterfly wings. Proceedings of SPIE, 4438(May 2011), 85-95.

Vukusic P, Sambles JR, Lawrence CR (2000). Colour mixing in wing scales of a butterfly. Nature, 404(6777), 457.

Vukusic P, Sambles JR, Lawrence CR. (2004). Structurally assisted blackness in butterfly scales. Proceedings of the Royal Society of London. B, 271 Suppl, S237-9.

Vukusic P, Sambles JR. (2003). Photonic structures in biology. Nature, 424(6950), 852-5.

Vukusic P, Stavenga DG. (2009). Physical methods for investigating structural colours in biological systems. Journal of the Royal Society, Interface, 6 Suppl 2(January), S133-48.

Ward BW, Notte JA, Economou NP. (2006). Helium ion microscope : A new tool for nanoscale microscopy and metrology. Journal of Vacuum Science and Technology B, 24(6), 2871-2874.

Watanabe K, Hoshino T, Kanda K, Haruyama Y, Matsui S. (2005). Brilliant blue observation from a Morpho-butterfly-scale quasi-structure. Japanese Journal of Applied Physics, Part 1(1), 44.

Wells OC (1960). Correction of errors in electron stereomicroscopy. British Journal of Applied Physics, 11(5), 199-201.

Wohlgemuth M, Yufa N, Hoffman J, Thomas EL. (2001). Triply Periodic Bicontinuous Cubic Microdomain Morphologies by Symmetries. Macromolecules, 34(17), 6083-6089.

Yoshida, A, Motoyama, M, Kosaku, A, Miyamoto, K. (1996). Nanoprotuberance Array in the Transparent Wing of a Hawkmoth, Cephonodes hylas. Zoological Science, 13(4), 525-526.

Yoshioka S, Nakano T, Nozue Y, Kinoshita S. (2008). Coloration using higher order optical interference in the wing pattern of the Madagascan sunset moth. Journal of the Royal Society, Interface, 5(21), 457-64.

Yoshioka S, Kinoshita S. (2006). Single-scale spectroscopy of structurally colored butterflies: measurements of quantified reflectance and transmittance. Journal of the Optical Society of America. A, Optics, 23(1), 134-41.